

# Decouple to Reconstruct: High Quality UHD Restoration via Active Feature Disentanglement and Reversible Fusion

Yidi Liu<sup>1,2</sup>, DongLi<sup>1</sup>, Yuxin Ma<sup>1</sup>, Jie Huang<sup>1</sup>, Wenlong Zhang<sup>2†</sup>, Xueyang Fu<sup>1†</sup>, Zheng-jun Zha<sup>1</sup>

<sup>1</sup>University of Science and Technology of China, <sup>2</sup>Shanghai AI Laboratory

liuyidi2023@mail.ustc.edu.cn, xyfu@ustc.edu.cn <sup>†</sup> Corresponding Author

## Abstract

*Ultra-high-definition (UHD) image restoration often faces computational bottlenecks and information loss due to its extremely high resolution. Existing studies based on Variational Autoencoders (VAE) improve efficiency by transferring the image restoration process from pixel space to latent space. However, degraded components are inherently coupled with background elements in degraded images, both information loss during compression and information gain during compensation remain uncontrollable. These lead to restored images often exhibiting image detail loss and incomplete degradation removal. To address this issue, we propose a Controlled Differential Disentangled VAE, which utilizes Hierarchical Contrastive Disentanglement Learning and an Orthogonal Gated Projection Module to guide the VAE to actively discard easily recoverable background information while encoding more difficult-to-recover degraded information into the latent space. Additionally, we design a Complex Invertible Multiscale Fusion Network to handle background features, ensuring their consistency, and utilize a latent space restoration network to transform the degraded latent features, leading to more accurate restoration results. Extensive experimental results demonstrate that our method effectively alleviates the information loss problem in VAE models while ensuring computational efficiency, significantly improving the quality of UHD image restoration, and achieves state-of-the-art results in six UHD restoration tasks with only 1M parameters.*

## 1. Introduction

With the widespread adoption of 4K display devices, ultra-high-definition (UHD) image restoration has become a key challenge in the field of computer vision. Traditional pixel-level processing methods are limited by the high-resolution characteristics of UHD images, resulting in significant computational bottlenecks [18, 27, 29, 37, 44].

To alleviate the computational burden of UHD image pro-

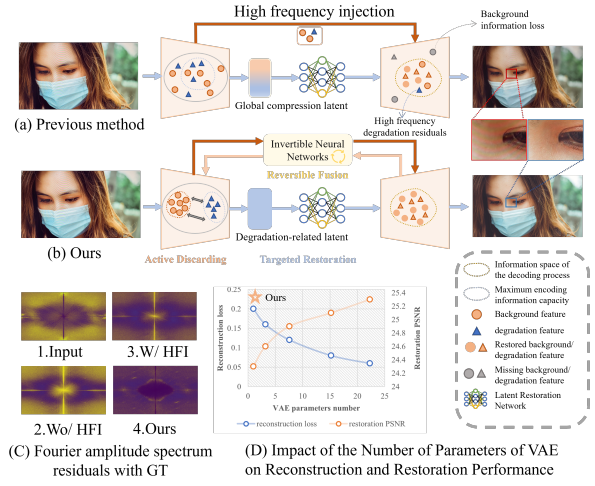


Figure 1. (a) Previous methods based on VAE suffered from irreversible background information loss due to global compression of the input image. Although additional High Frequency Injection (HFI) can partially mitigate the loss of high-frequency details, it also leads to residual high-frequency degradation. (b) Our proposed CD<sup>2</sup>-VAE decouples background and degradation features and achieves a balance between background consistency and low residual degradation through a dual-path reconstruction structure. (c) As the number of parameters in the VAE model increases, the reconstruction capability improves, leading to better restoration results. However, the excessive parameter count does not meet the lightweight requirements for UHD image restoration.

cessing, previous methods generally place the core restoration computation in the downsampled space of the original image. UHDfour [16] and UHDformer [27] reduce the spatial dimension of the original input through PixelUnshuffle [22] and convolution operations, while LMAR [35] designs a learning-based resampling operator. Clearly, the dimensionality reduction process leads to the loss of most of the information in the original image. Therefore, these methods often use a more lightweight network to process the image at its original resolution, thereby compensating for the information lost in the downsampling branch. DreamUHD [18] develops a VAE framework that outperforms

standard downsampling in compression efficiency. Its High-Frequency Injection strategy directly mitigates information loss during VAE encoding.

Since degraded components are inherently coupled with background elements in degraded images, both information loss during compression and information gain during compensation remain uncontrollable. These lead to restored images often exhibiting image detail loss and incomplete degradation removal. Consequently, UHD restoration still faces a significant challenge: *the controllability of information compression and compensation*. This issue can be explained through three key aspects. **(1) Representation bottleneck.** VAEs lose multi-frequency signals through non-discriminatory compression (Figure 1(c2)), despite their information retention capability. While enhancing VAE architecture lowers reconstruction errors (Figure 1(d)) and boosts restoration quality, the enlarged parameter size contradicts UHD restoration’s efficiency requirements. **(2) Entangled feature lost.** Compression eliminates both degraded/clean features due to their coupling (Figure 1(a)). This causes (i) Incomplete compensation (high-frequency recovered but low-frequency lost, Figure 1(c3)) and (ii) Latent space over-crowding with clean features, diverting restoration efforts to irrelevant data. **(3) Uncertainty in the compensation process.** Since the compensation information is derived from the original image, which also contains tightly coupled degraded and background components (Figure 1(a)), the injected compensation features introduce degraded components, leading to degradation artifacts in the restoration results.

In this work, we aim to achieve controllable information loss compression and predictable information compensation through feature decoupling. We presents the Decoupled Dual-path UHD Restoration Network(D<sup>2</sup>R-UHDNet), a novel framework for UHD image restoration based on the Active Discarding-Targeted Restoration paradigm. Using Controlled Differential Disentangled Variational Autoencoder(CD<sup>2</sup>-VAE), the method decomposes the degraded input into two components: degradation-dominant latent space ( $z_{\text{deg}}$ ) and background-dominant features ( $\{F_{\text{bg}}^l\}_{l=1}^L$ ). This enables dual-path restoration: the Latent Restoration Network (LaReNet) maps the degraded latent  $z_{\text{deg}}$  to the clean latent  $z_{\text{clean}}$ , while the Complex Invertible Multiscale Fusion Network (CIMF-Net) ensures information preservation and facilitates efficient background reconstruction through multi-scale fusion.

The CD<sup>2</sup>-VAE architecture establishes a joint optimization framework through a Hierarchical Contrastive Disentanglement Learning (Hi-CDL) strategy and an Orthogonal Gated Projection Module (OrthoGate). The Hi-CDL strategy employs multi-scale contrastive learning between clean and degraded features, enforcing the VAE to progressively disentangle background information while iteratively encoding retained features for degradation extraction. Concurrently,

the OrthoGate module implements orthogonal projection within the Stiefel manifold space, mathematically guaranteeing minimal mutual information between decoupled feature subspaces [1]. The synergistic effect of both components enables more precise feature disentanglement.

This work does not aim to “suppress” information loss by enhancing the representational capacity of the VAE but instead guides the VAE to actively discard easily recoverable information through feature disentanglement. Simultaneously, it effectively encodes the harder-to-recover information into the latent space. By increasing the density of degraded latent information while minimizing the compression loss of background features, our method enables a divide-and-conquer manner for background-dominant and degradation-dominant features. This approach not only alleviates information loss but also maintains the lightweight nature of the network, meeting the practical requirements of UHD restoration. Our contributions are summarized as follows:

- We propose D<sup>2</sup>R-UHDNet for UHD image restoration, using the Active Discarding and Targeted Restoration paradigm to transform VAE’s information loss into task-driven discarding, balancing degraded information removal and background preservation in a efficient manner.
- We propose CD<sup>2</sup>-VAE, which introduces Hi-CDL and OrthoGate. These components enable effective feature disentanglement of degraded inputs.
- We propose CIMF-Net, which uses invertibility to ensure consistent information across multi-scale background-dominant features and employs complex operations for efficient cross-scale interaction. Our method achieves state-of-the-art results in six UHD restoration tasks with only 1M parameters.

## 2. Related Works

### 2.1. Variational Autoencoder.

Recently, the compact and informative latent space of VAEs has garnered increasing attention, leading to a wide range of applications. Latent Diffusion [21] transfers the diffusion process from pixel space to latent space, improving image generation efficiency. Old Photo Restoration (OPR) [26] reduces the domain gap between synthetic and real degradation in the latent space, enhancing model generalization for real old photos.

DreamUHD is the first to use latent space compression for UHD image restoration, improving efficiency. To address high-frequency loss in VAE encoding, it introduces a high-frequency injection mechanism, reducing edge blurring. However, this injection also causes residual degradation and fails to suppress mid-to-low frequency information loss. To solve this, we propose a Controlled Differential Disentangled VAE that decouples features, making information loss

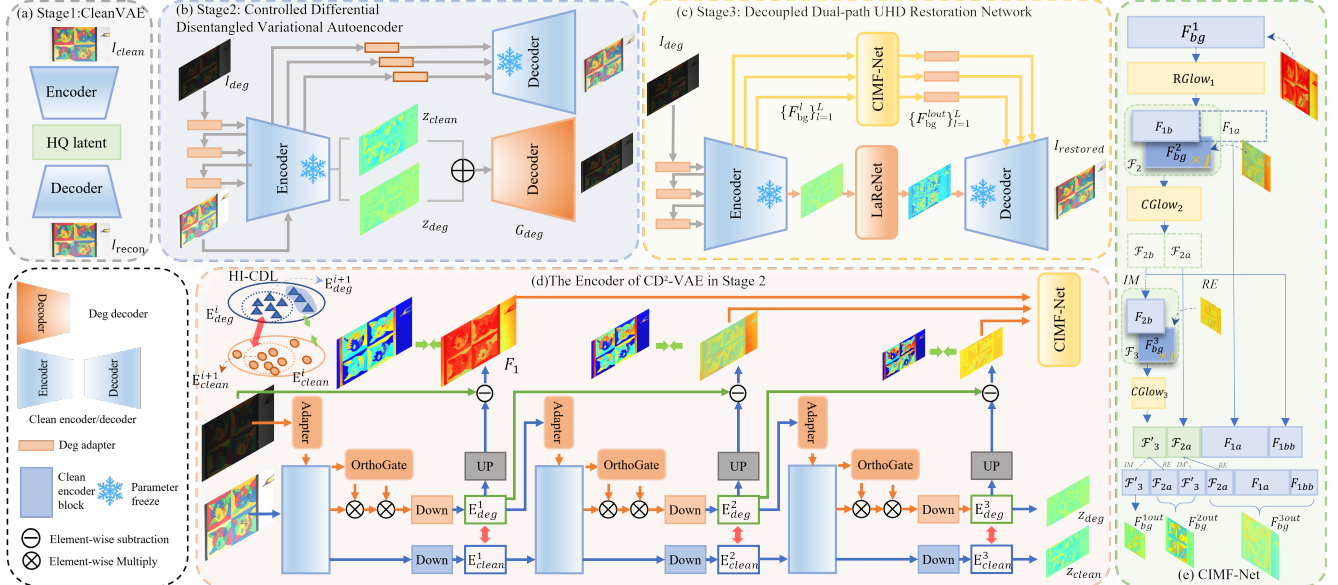


Figure 2. The framework of our method: (a) In the first stage, CleanVAE is trained on clean images. (b) In the second stage, CD2-VAE is trained based on feature decoupling constraints. (c) In the third stage, D2R-UHDNet is constructed for image restoration using CD2-VAE.(d) Detailed illustration of the second stage CD2-VAE encoding process. (e) Structure of CIMF-Net.

controllable and balancing degradation removal with information retention.

## 2.2. Ultra-High-Definition Restoration

Recent advancements in image restoration technologies [5, 11, 17, 32, 37] have improved performance at traditional resolutions but struggle with computational efficiency and performance when applied to UHD images. To meet the increasing demand for UHD image processing, methods such as bilateral learning for dehazing [41], multi-scale networks for video deblurring [9], Fourier embedding for low-light enhancement [16], and wavelet-based Mamba networks [44] have been proposed.

Recently, general architectures for UHD image restoration have rapidly developed, addressing multiple restoration problems with a unified structure. To mitigate the large computational cost of UHD image processing, UHDformer [27] constructs two branches for high and low resolutions using PixelShuffle, UHDDIP integrates gradient and normal priors through an external model [29], and DreamUHD [18] introduces latent space modeling with VAE to enhance restoration efficiency. In this context, the prior in UHDDIP requires an additional model for computation, which makes it less efficient. In contrast, UHDformer and DreamUHD aim to allocate computationally intensive structures to the downsampled space while assigning lighter structures to the original space, thus improving efficiency. However, performing downsampling compression on all the information in the image leads to irreversible information loss, and the lightweight structures applied to the original space are often too simplis-

tic, which can result in residual degradation in the restored image. In this paper, D2R-UHDNet introduces an Active Discarding and Targeted Restoration paradigm, which avoids the uncontrollable loss of information during downsampling, significantly enhancing the performance of UHD restoration tasks.

## 3. Method

### 3.1. Overview

This paper proposes the Decoupled Dual-path UHD Restoration Network (D2R-UHDNet), whose core objective is to achieve efficient and high-quality restoration of Ultra-High Definition (UHD) images through guided feature disentanglement and dual-path collaborative restoration.

Our overall framework is shown in Figure 3. In the first stage, we train a CleanVAE on clean images for image reconstruction, as shown in Figure 3(a). Next, we introduce feature decoupling constraints to separately reconstruct clean and degraded images, resulting in the trained CD2-VAE, as shown in Figure 3(b). In the third stage, D2R-UHDNet is constructed based on CD2-VAE for UHD image restoration. The detailed encoding process of CD2-VAE and CIMF-Net for handling multi-scale background-dominated features in D2R-UHDNet are shown in Figure 3(d) and Figure 3(e), respectively. We will provide a detailed introduction to these processes in Sec. 3.2 and Sec. 3.3.

### 3.2. Controlled Differential Disentangled VAE

Unlike traditional VAEs, CD<sup>2</sup>-VAE introduces Hierarchical Contrastive Disentanglement Learning (Hi-CDL) and the Orthogonal Gated Projection Module (OrthoGate), transforming the encoding process into a controllable information filtering operation: background features that are easy to restore are discarded first, while degradation components requiring targeted restoration are carefully preserved.

Given the degraded Ultra-High Definition (UHD) image  $I_{\text{deg}} \in \mathbb{R}^{H \times W \times 3}$ , CD<sup>2</sup>-VAE utilizes Hi-CDL and OrthoGate to progressively disentangle background features  $\{F_{\text{bg}}^l\}_{l=1}^L$ , while retaining the degraded latent encoding  $z_{\text{deg}} \in \mathbb{R}^{\frac{H}{2^L} \times \frac{W}{2^L} \times 3}$ .

#### 3.2.1. Hierarchical Contrastive Disentanglement

To drive the progressive disentanglement of degraded and background features across multiple scales, this paper introduces Hierarchical Contrastive Disentanglement Learning (Hi-CDL). The core idea is to explicitly guide the encoder by comparing the cross-level similarity between degraded features and clean reference features, encouraging the active discard of background information irrelevant to degradation at each layer, while preserving the information relevant to the degradation.

For the  $i$ -th layer encoder, the input degraded and clean features are  $E_{\text{deg}}^{i-1}, E_{\text{clean}}^{i-1} \in \mathbb{R}^{h \times w \times c}$ , and the output of this layer is  $E_{\text{deg}}^i, E_{\text{clean}}^i \in \mathbb{R}^{\frac{h}{2} \times \frac{w}{2} \times 2c}$ , where features are progressively compressed during the encoding process. We aim for the CD<sup>2</sup>-VAE to progressively disentangle  $E_{\text{deg}}^{i-1}$  from background-irrelevant features during encoding and increase the similarity between  $E_{\text{deg}}^i$  and  $E_{\text{clean}}^i$ . Simultaneously, to ensure that the information reduced from  $E_{\text{deg}}^{i-1}$  to  $E_{\text{deg}}^i$  is mainly background information, we aim to reduce the feature discrepancy between  $E_{\text{deg}}^{i-1}$  and  $E_{\text{deg}}^i$ , while enhancing their similarity to the corresponding background features. This process can be expressed as follows:

$$\begin{aligned} \mathcal{L}_{\text{contrast}}^i &= -\log \frac{\exp(s_{\text{pos}}^i / \tau_i)}{\exp(s_{\text{pos}}^i / \tau_i) + \exp(s_{\text{neg}}^i / \tau_i) + \epsilon}, \\ s_{\text{neg}}^i &= \text{sim}(E_{\text{deg}}^i, E_{\text{clean}}^i), \\ s_{\text{pos}}^i &= \text{sim}\left(E_{\text{deg}}^{i-1} - \text{UP}(E_{\text{deg}}^i), E_{\text{clean}}^{i-1}\right), \end{aligned} \quad (1)$$

where  $\text{sim}(\cdot)$  denotes the cosine similarity calculation, and  $\text{UP}(\cdot)$  represents the Pixel Shuffle and Channel Duplication operation,  $\epsilon$  is a numerical stabilization term.  $\tau_i$  is the temperature coefficient. As the layer  $i$  increases, we gradually reduce  $\tau_i$  to strengthen the feature disentanglement, allowing the disentanglement process to shift from global information to fine-grained details.

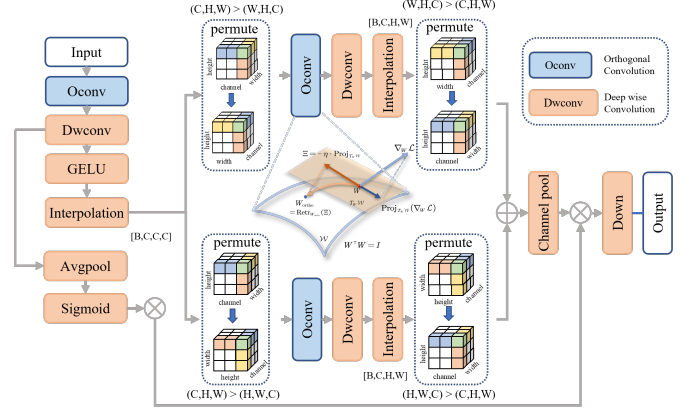


Figure 3. Orthogonal Gated Projection Module.

#### 3.2.2. Orthogonal Gated Projection Module

The Hi-CDL strategy explicitly constrains the disentanglement process of CD<sup>2</sup>-VAE by constructing a loss function. Additionally, we introduce the Orthogonal Gated Projection Module (OrthoGate) to control the flow of information during the encoding process.

Specifically, to further promote feature disentanglement, we construct a orthogonal pointwise convolution(O<sub>conv</sub>) based on the Stiefel manifold constraint [1], with the convolution parameters denoted as  $W_{\text{ortho}}$ . Due to the Stiefel manifold constraint, this matrix satisfies the orthogonality condition:

$$W = \{W \in \mathbb{R}^{C \times C} \mid W^T W = I\} \quad (2)$$

The parameters of this convolution are optimized using a Riemannian gradient-based update strategy to satisfy the Stiefel manifold constraint:

$$\begin{aligned} W_{\text{ortho}} &\leftarrow \text{Retr}_{W_{\text{ortho}}}(-\eta \cdot \text{Proj}_{T_W W}(\nabla_W \mathcal{L})), \\ \text{Proj}_{T_W W}(\nabla_W \mathcal{L}) &= \nabla_W \mathcal{L} - W \cdot \text{sym}(W^T \nabla_W \mathcal{L}), \end{aligned} \quad (3)$$

where, Retr denotes the retraction,  $\text{Proj}_{T_W W}(\cdot)$  is the tangent space projection operator,  $\mathcal{L}$  is the loss function, and  $\text{sym}(A) = \frac{A+A^T}{2}$  represents the symmetrization of the matrix  $A$ .

First, we construct a channel disentanglement gating based on O<sub>conv</sub>. At the  $i$ -th layer,  $E_{\text{deg}}^i$ , after passing through the Encoder block, becomes  $E_{\text{deg}}^{i'} \in \mathbb{R}^{h \times w \times 2c}$  before the downsampling step. We first use O<sub>conv</sub> to reduce the inter-channel feature correlation, and then apply depthwise convolution to enable spatial dimension interaction while preserving the channel disentanglement. Next, we apply global average pooling followed by the Sigmoid activation function to obtain the channel gating factor  $C_{\text{gate}} \in \mathbb{R}^{1 \times 1 \times 2c}$ . This factor is then dot-multiplied with  $E_{\text{deg}}^{i'}$  to obtain the output of the channel disentanglement gating,  $E_{\text{deg}}^i$ . This process

can be expressed as follows:

$$\begin{aligned} E_{deg}^{i^1} &= D_{conv} O_{conv}(E_{deg}^{i'}), \\ C_{gate} &= \mathcal{S}(\text{GAP}(E_{deg}^{i'}))), \\ E_{deg}^c &= C_{gate} \odot E_{deg}^{i'}, \end{aligned} \quad (4)$$

where,  $\mathcal{S}(\cdot)$  denotes the Sigmoid activation function,  $\text{GAP}(\cdot)$  represents global average pooling,  $D_{conv}(\cdot)$  refers to depthwise convolution, and  $\odot$  denotes the element-wise dot product operation.

After disentangling the features in the channel dimension, we further disentangle the spatial dimensions. First, we interpolate  $E_{deg}^{i^1}$  so that its spatial dimensions match the channel dimension, resulting in  $E_{deg}^{i^2} \in \mathbb{R}^{c \times c \times c}$ . Then, we perform a permute operation on  $E_{deg}^{i^2}$ , moving the  $h$  and  $w$  dimensions to the channel dimension, followed by orthogonal convolution and depthwise convolution. After that, we apply interpolation and permute operations to restore the features to their original dimensions, obtaining  $E_{deg}^{i^2} \in \mathbb{R}^{h \times w \times c}$ . This process can be expressed as follows:

$$\begin{aligned} E_{deg}^{i^{h1}} &= D_{conv}(O_{conv}(\text{Permute}_{h,w,c \rightarrow c,h,w}(\mathcal{I}_p(E_{deg}^{i^1}, \mathbb{R}^{c \times c \times c})))), \\ E_{deg}^{i^{h2}} &= \text{Permute}_{h,w,c \rightarrow c,h,w}(\mathcal{I}_p(E_{deg}^{i^{h1}}, \mathbb{R}^{h \times w \times c}))), \end{aligned} \quad (5)$$

where  $\mathcal{I}_p(\cdot, \mathbb{R}^{m \times n \times c})$  is an interpolation operation that adjusts the input dimensions to  $\mathbb{R}^{m \times n \times c}$ , and  $\text{Permute}_{h,w,c \rightarrow c,h,w}$  denotes the permutation operation that rearranges the dimensions from  $(h, w, c)$  to  $(c, h, w)$ . Similarly, by applying  $\text{Permute}_{h,w,c \rightarrow c,w,h}$ , we obtain  $E_{deg}^{i^{w2}}$  through the same process.

Subsequently, we add  $E_{deg}^{i^{h2}}$  and  $E_{deg}^{i^{w2}}$ , and perform channel pooling to obtain the spatial gating factor  $S_{gate} \in \mathbb{R}^{h \times w \times 1}$ . This factor is then element-wise multiplied with  $E_{deg}^{i^c}$  to yield the spatial disentanglement gating output  $E_{deg}^{i^p}$ . Finally,  $E_{deg}^{i^p}$  undergoes downsampling to produce the output of the Encoder for this layer,  $E_{deg}^{i+1}$ . This process can be expressed as follows:

$$\begin{aligned} S_{gate} &= \mathcal{S}(\mathcal{C}(E_{deg}^{i^{h2}} + E_{deg}^{i^{w2}})), \\ E_{deg}^{i+1} &= \text{Down}(E_{deg}^{i^c} \odot S_{gate}) \end{aligned} \quad (6)$$

where  $\mathcal{C}(\cdot)$  represents the channel average pooling operation, and  $\text{Down}$  denotes the downsampling module in the encoder block.

### 3.3. Complex Invertible Multiscale Fusion Network

The multi-scale background features  $\{F_{bg}^l\}$  are input into CIMF-Net, where cross-scale information fusion is achieved through invertible computation in the complex domain. The

degraded latent encoding  $z_{deg}$  is input into a lightweight latent-space restoration network, mapping it to the clean distribution. The restored background features  $\{F_{bg}^{lout}\}$  and the clean encoding  $z_{clean}$  are then input into the decoder  $G_{dec}$  to generate the final restored image  $I_{restored}$ .

By combining complex domain representation with invertible computation, CIMF-Net enables efficient cross-scale interaction and consistent information transfer. We employ GLOW [12] as the invertible module within CIMF-Net.

For multi-scale background features  $\{F_{bg}^l\}_{l=1}^L$ , we begin with  $F_{bg}^1 \in \mathbb{R}^{h \times w \times c}$ , which is processed by the real-valued invertible network Real-GLOW to produce the output  $F_{bg}^{1'} \in \mathbb{R}^{h \times w \times c}$ . Next, we apply PixelShuffle and channel splitting to  $F_{bg}^{1'} \in \mathbb{R}^{h \times w \times c}$ , obtaining  $F_{bg}^{1^1}, F_{bg}^{1^2} \in \mathbb{R}^{\frac{h}{2} \times \frac{w}{2} \times c}$ .

Then,  $F_{bg}^{1^1}$  is output directly, while  $F_{bg}^{1^2}$  and  $F_{bg}^{2^1}$  are combined as the real and imaginary parts, respectively, and passed into the next layer of the complex invertible network Complex-GLOW to produce the output  $F_{bg}^{1^{2'}} + F_{bg}^{2'}j$ . We then apply PixelShuffle and channel splitting again, resulting in  $F_{bg}^{1^{21}} + F_{bg}^{21}j, F_{bg}^{1^{22}} + F_{bg}^{22}j \in \mathbb{R}^{\frac{h}{4} \times \frac{w}{4} \times 4c}$ . Finally,  $F_{bg}^{2^2}$  and  $F_{bg}^{3^1}$  are combined as the real and imaginary parts, respectively, and passed into another layer of Complex-GLOW, resulting in  $F_{bg}^{2^{2'}} + F_{bg}^{3'}j$ . After all features are processed, we assemble them into the final outputs  $F_{bg}^{1out}, F_{bg}^{2out}, F_{bg}^{3out}$ . This process can be expressed as Algorithm 1, where  $\mathcal{PS}$  denotes the PixelUnshuffle and channel split operations, and  $\mathcal{A}$  represents the feature recomposition operation, where Pixelshuffle and channel concatenation are employed to reconstruct the features at each scale into their original shape.

---

#### Algorithm 1 Complex Invertible Multiscale Fusion (CIMF)

**Input:** Multi-scale features  $\{F_l\}_{l=1}^L$

**Output:** Fused feature  $F_{out}$

**Level 1 Processing:**

$$F'_1 \leftarrow \text{RealGLOW}(F_1); (F_{1a}, F_{1b}) \leftarrow \mathcal{PS}(F'_1)$$

$$F_{\text{keep}} \leftarrow F_{\text{keep}} \cup \{F_{1a}\}; F_{\text{pass}} \leftarrow F_{1b}$$

**Intermediate Levels:** **for**  $l \leftarrow 2$  **to**  $L - 1$  **do**

$$\begin{aligned} \mathcal{F}_l &\leftarrow \text{ComplexGLOW}(F_{\text{pass}} + jF_l) \quad \triangleright \text{Complex fusion} \\ (\mathcal{F}_{la}, \mathcal{F}_{lb}) &\leftarrow \mathcal{PS}(\mathcal{F}_l) \\ F_{\text{keep}} &\leftarrow F_{\text{keep}} \cup \{\mathcal{F}_{la}, \text{Re}(\mathcal{F}_{lb})\} \\ F_{\text{pass}} &\leftarrow \text{Im}(\mathcal{F}_{lb}) \end{aligned}$$

**end**

**Final Level Processing ( $l = L$ ):**

$$\mathcal{F}_L \leftarrow \text{ComplexGLOW}(F_{\text{pass}}, F_L)$$

$$F_{\text{keep}} \leftarrow F_{\text{keep}} \cup \{\text{Re}(\mathcal{F}_L), \text{Im}(\mathcal{F}_L)\}$$

**Assembly:**  $\{F_l^{out}\}_{l=1}^L \leftarrow \mathcal{A}(F_{\text{keep}}) \triangleright \text{Recomposition}$

**return**  $\{F_l^{out}\}_{l=1}^L$

---

Complex-GLOW consists primarily of the Complex Invertible  $1 \times 1$  Convolution, Complex ActNorm, and Complex Affine Coupling. First, we construct the core operator for complex computation, the complex convolution. For a complex convolution kernel  $W_{\text{complex}} = W_{\text{re}} + jW_{\text{im}}$ , the computation process is as follows:

$$\begin{aligned}\text{Re}(\mathcal{F}_{\text{out}}) &= (\text{Re}(\mathcal{F}) * W_{\text{re}} - \text{Im}(\mathcal{F}) * W_{\text{im}}) \\ \text{Im}(\mathcal{F}_{\text{out}}) &= (\text{Re}(\mathcal{F}) * W_{\text{im}} + \text{Im}(\mathcal{F}) * W_{\text{re}})\end{aligned}\quad (7)$$

Based on the complex convolution kernel, we apply polar decomposition to impose a unitary matrix constraint on  $W_{\text{complex}}$ , ensuring its invertibility:

$$\begin{aligned}W_{\text{complex}}^\dagger W_{\text{complex}} &= I \Rightarrow |\det(W_{\text{complex}})| = 1, \\ W_{\text{complex}} &= U \cdot \Sigma, \quad U^\dagger U = I, \quad \Sigma \succeq 0,\end{aligned}\quad (8)$$

The real and imaginary parts of the complex features are separately normalized using affine normalization:

$$\begin{aligned}\text{Re}(\mathcal{F}_{\text{out}}) &= \frac{\text{Re}(\mathcal{F}) - \mu_{\text{re}}}{\sigma_{\text{re}}} \cdot s_{\text{re}} + b_{\text{re}} \\ \text{Im}(\mathcal{F}_{\text{out}}) &= \frac{\text{Im}(\mathcal{F}) - \mu_{\text{im}}}{\sigma_{\text{im}}} \cdot s_{\text{im}} + b_{\text{im}}\end{aligned}\quad (9)$$

where,  $\{\mu_{\text{re}}, \mu_{\text{im}}\}$  and  $\{\sigma_{\text{re}}, \sigma_{\text{im}}\}$  are the per-channel statistics, while  $\{s_{\text{re}}, s_{\text{im}}\}$  and  $\{b_{\text{re}}, b_{\text{im}}\}$  are the learnable parameters.

The input complex features  $\mathcal{F}$  are split into  $\mathcal{F}_1$  and  $\mathcal{F}_2$ , and the scale  $\gamma$  and offset  $\beta$  are predicted using the complex neural network ComplexNN:

$$\begin{aligned}\gamma_1 + j\gamma_2, \beta_1 + j\beta_2 &= \text{ComplexNN}(\mathcal{F}_1), \\ \mathcal{F}'_2 &= \mathcal{F}_2 \odot (\gamma_1 + j\gamma_2) + (\beta_1 + j\beta_2),\end{aligned}\quad (10)$$

The ComplexNN is composed of a complex convolution module. The output is  $\mathcal{F}_{\text{out}} = \text{Concat}(\mathcal{F}_1, \mathcal{F}'_2)$ , and the inverse transformation can be explicitly computed.

### 3.4. Latent Restoration Network

For the degraded latent  $z_{\text{deg}} \in \mathbb{R}^{\frac{H}{2L} \times \frac{W}{2L} \times 3}$ , we construct the Latent Restoration Network (LaReNet) to map the degraded latent  $z_{\text{deg}}$  to the clean latent  $z_{\text{clean}}$ . This network can be constructed using a simple image restoration network module. This work uses SFHformer [11], while other image restoration network modules are explored in the ablation study.

## 4. Experiment

### 4.1. Experimental Setup

For single degradation removal, we followed the dataset settings from DreamUHD [18], using UHD-LL [16] for low-light enhancement, UHD-Haze [41] for dehazing, UHD-Blur [7] for deblurring, and UHD-M [36] for de-moiréing.

More detailed dataset settings and additional visual comparisons are provided in the supplementary material. FLOPs are computed with an input size of  $256 \times 256$ , and inference time is tested at 4K resolution on an RTX 3090.

## 4.2. Comparison with State-of-the-Art Methods

### 4.2.1. Low-Light Image Enhancement Results

The results for Low-Light Image Enhancement are shown in Figure 4(a). Compared to other methods, our approach preserves text details under extremely low light conditions, yielding clearer results. The quantitative comparison results are shown in Tab. 1, where our method achieves the best performance while maintaining lightweight design.

### 4.2.2. Image Dehazing Results

The visual comparison results for Image Dehazing are shown in Figure 4(b). Compared to other methods, our approach results in less haze residue, yielding cleaner results. The quantitative comparison results, as shown in Tab. 2, demonstrate a 0.68dB PDNR improvement over the previous SOTA results, validating the effectiveness of our method.

### 4.2.3. Image Deblurring Results

The visual comparison results for Image Deblurring are shown in Figure 4(c). Compared to other methods, our method better restores motion-induced blur artifacts. The quantitative comparison results, as shown in Tab. 3, demonstrate that our method achieves optimal performance.

### 4.2.4. Image Demoiréing Results

The visual comparison results for Image Demoiréing are shown in Figure 4(d). Compared to other methods, our approach more thoroughly removes moiré patterns from the image. The quantitative comparison results, as shown in Tab. 3, demonstrate a 0.68dB PSNR performance improvement over previous methods.

### 4.2.5. Four Degradations All in one Results

The Active Discarding and Targeted Restoration paradigm proposed in this paper gradually decouples background-dominated information unrelated to degradation from the degraded images, making it naturally suited for the *All in One* task, where a single model addresses multiple degradation scenarios. Without any additional design, as shown in Tab. 5, our method still achieves the best results for the UHD All in One task with four degradation types, further validating the effectiveness of our approach. For more details on the All in One experimental setup and the comparison results for six types of degradation, please refer to the supplementary.

## 5. Ablation Study

In this section, we conduct ablation experiments on the UHD image deblurring task using CD<sup>2</sup>-VAE, CIMF-Net, and LaReNet to validate their effectiveness.

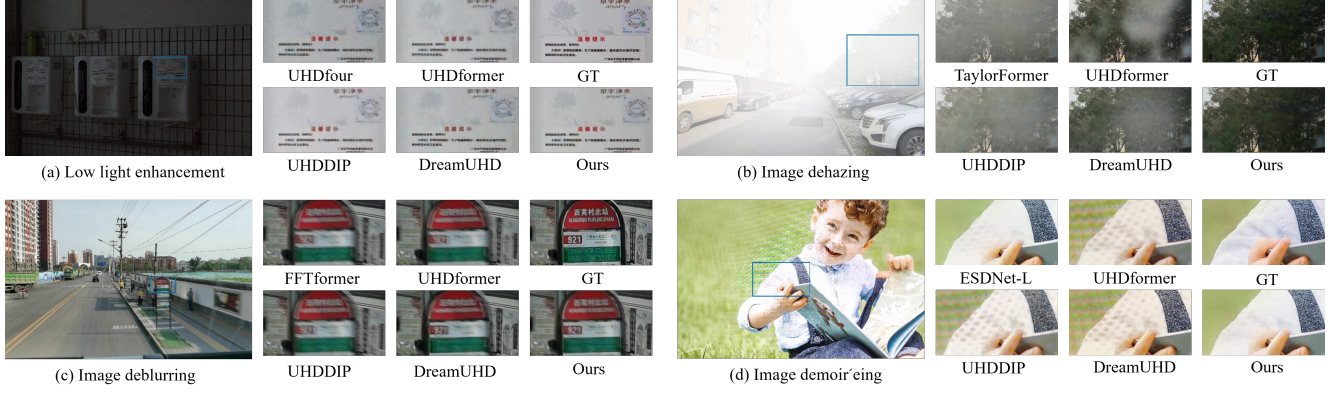


Figure 4. A comparison of visual results for four types of degradation removal with other state-of-the-art (SOTA) all-in-one methods.

Table 1. Quantitative results of low-light image enhancement.

Method	FS	Params(M)	PSNR	SSIM	LIPIPS
Restormer [37]	✗	26.1	21.54	.843	.3608
LLformer [30]	✗	13.2	24.06	.858	.3516
UHDFour [15]	✓	17.5	26.22	.900	.2390
UHDFormer [27]	✓	0.3393	27.11	.927	.2240
LMAR [35]	✓	1.965	26.27	.919	.2248
UHDDIP [28]	✓	0.81	26.74	.928	.2076
DreamUHD [18]	✓	1.215	<b>27.72</b>	<b>.928</b>	<b>.2051</b>
Ours	✓	1.008	<b>27.94</b>	<b>.934</b>	<b>.2041</b>

Table 2. Quantitative results of image dehazing.

Method	FS	Params(M)	PSNR	SSIM	LIPIPS
Restormer [37]	✗	26.1	12.72	.693	.4560
Uformer [32]	✗	20.6	19.83	.921	.4220
DehazeFormer[23]	✗	2.5	15.37	.737	.3998
TaylorFormer [20]	✗	2.7	20.99	.919	.3124
UHDFormer [27]	✓	0.3393	22.58	.942	.1188
UHDDIP [28]	✓	0.81	<b>24.69</b>	<b>.952</b>	<b>.1049</b>
DreamUHD [18]	✓	1.215	24.36	.945	.1176
Ours	✓	1.008	<b>25.37</b>	<b>.955</b>	<b>.1044</b>

Table 3. Quantitative results of image deblurring.

Method	FS	Params(M)	PSNR	SSIM	LIPIPS
Restormer [37]	✗	26.1	25.21	.752	.3695
Uformer [32]	✗	20.6	25.26	.751	.3851
Stripformer [25]	✗	19.7	25.05	.750	.3740
FFTformer [13]	✗	16.6	25.41	.757	.3708
UHDFormer [27]	✓	0.3393	28.82	.844	.2350
UHDDIP [28]	✓	0.81	<b>29.51</b>	<b>.858</b>	<b>.2127</b>
DreamUHD [18]	✓	1.456	29.33	.852	.2222
Ours	✓	1.008	<b>29.84</b>	<b>.861</b>	<b>.2124</b>

Table 4. Quantitative results of image demoir'eing.

Method	FS	Params(M)	PSNR	SSIM	LIPIPS
FHDe <sup>2</sup> Net[37]	✗	13.571	20.33	.749	.3519
ESDNet [36]	✓	5.93	22.11	.795	.2551
ESDNet-L [36]	✓	10.62	22.42	.798	<b>.2454</b>
UHDFormer [27]	✓	0.3393	21.96	.833	.3854
UHDDIP [28]	✓	0.81	22.06	.802	.3822
DreamUHD [18]	✓	1.456	<b>23.24</b>	<b>.843</b>	.3259
Ours	✓	1.008	<b>23.92</b>	<b>.851</b>	<b>.2842</b>

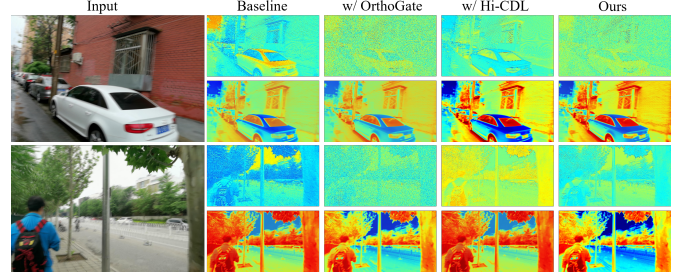


Figure 5. Feature visualization of CD<sup>2</sup>-VAE ablation experiments. The first row shows the encoded latent representation, and the second row shows the discarded information during encoding.

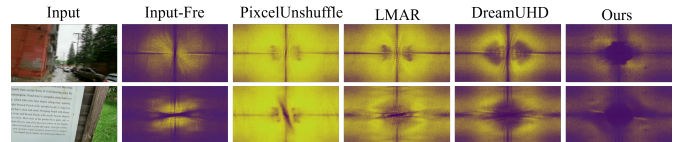


Figure 6. Frequency spectrum residual maps of different compression methods compared to GT, with "Input-fre" representing the residual map between input and GT.

## 5.1. Controlled Differential Disentangled VAE

For the ablation experiments of the proposed CD<sup>2</sup>-VAE, as shown in Tab. 6, it can be seen that the two decoupling mechanisms introduced in CD<sup>2</sup>-VAE, Hi-CDL and OrthoGate, significantly improve performance, with further enhancement achieved through their synergistic effect. We performed feature visualization of the latent and discarded information encoded by the VAE in all ablation experiments, with results shown in Figure 5. It can be observed that due to the deep coupling of degraded components and background components in the degraded images, the baseline method indiscriminately compresses all components, leading to uncontrollable information loss during the encoding process. After introducing Hi-CDL and OrthoGate, the infor-

Table 5. Comparison to state-of-the-art on four degradations. PSNR (dB,  $\uparrow$ ), SSIM ( $\uparrow$ ), and LPIPS ( $\downarrow$ ), and FS represents full-size 4K image inference. FLOPs are computed for an input size of  $256 \times 256$ . **Best** and **second best** performances are highlighted.

Method	FS	FLOPs	Params.	Low Light		Deblurring		Dehazing		Denoising			Average					
				UHD-LL	UHD-blur	UHD-haze	UHDN $_{\sigma=15}$	UHDN $_{\sigma=25}$	UHDN $_{\sigma=50}$	UHDN $_{\sigma=15}$	UHDN $_{\sigma=25}$	UHDN $_{\sigma=50}$	UHDN $_{\sigma=15}$	UHDN $_{\sigma=25}$	UHDN $_{\sigma=50}$			
AIRNet [14]	$\times$	301G	9M	19.24	.809	21.89	.757	18.37	.812	21.33	.887	20.78	.784	18.79	.475	20.07	.754	.2843
IDR [38]	$\times$	88G	15.3M	23.12	.910	24.67	.793	19.12	.768	27.48	.912	25.86	.872	24.57	.654	24.14	.822	.2684
PromptIR [19]	$\times$	158G	33M	23.44	.902	25.77	.782	19.97	.727	28.43	.924	26.74	.898	23.72	.584	24.68	.803	.2571
CAPTNet [10]	$\times$	25G	24.3M	23.96	.920	26.11	.798	19.46	.868	25.58	.865	23.24	.884	21.98	.508	23.39	.809	.3466
NDR-Restore [33]	$\times$	196G	36.9M	23.84	.894	24.25	.802	20.08	.892	25.62	.912	24.37	.897	22.94	.669	23.52	.846	.3126
Gridformer [31]	$\times$	367G	34M	23.12	.898	25.82	.783	19.24	.869	36.04	.937	31.72	.898	26.24	.623	27.03	.836	.3754
DiffUIR-L [40]	$\times$	10G	36.2M	21.56	.812	23.85	.743	18.28	.864	<b>36.84</b>	<b>.938</b>	<b>32.42</b>	.897	26.08	.648	26.51	.818	<b>.2564</b>
Histoformer [24]	$\times$	91G	16.6M	23.22	.908	25.62	.782	19.78	<b>.903</b>	26.88	.845	25.64	.874	23.13	.659	24.04	.829	.3524
adalIR [6]	$\times$	147G	28.7M	23.57	.916	<b>26.35</b>	<b>.801</b>	18.44	.901	32.84	.921	30.48	<b>.901</b>	<b>26.48</b>	<b>.672</b>	26.36	<b>.857</b>	.3429
HAIR [2]	$\times$	41G	29M	<b>25.75</b>	<b>.922</b>	25.78	.798	<b>20.00</b>	.894	35.54	.916	30.84	.878	26.26	.657	27.36	.847	.2822
UHDformer [27]	✓	3.0G	0.33M	23.22	.904	25.44	.782	19.48	.911	34.72	.942	30.27	.881	26.08	.653	26.53	.846	.2878
UHDDIP [29]	✓	2.2G	0.81M	22.32	.894	25.68	.792	19.84	.899	36.42	.922	29.33	.872	26.21	.652	26.63	.839	.2878
DreamUHD [18]	✓	4.1G	1.46M	24.23	.915	25.84	.808	19.92	.902	36.59	.927	31.64	.886	26.38	.657	<b>27.43</b>	.849	.2822
Ours	✓	4.0G	1.0M	<b>25.89</b>	<b>.924</b>	<b>26.42</b>	<b>.803</b>	<b>20.34</b>	<b>.914</b>	<b>37.13</b>	<b>.941</b>	<b>32.89</b>	<b>.904</b>	<b>26.54</b>	<b>.675</b>	<b>28.20</b>	<b>.860</b>	<b>.2523</b>

Table 6. Ablation Study of the CD<sup>2</sup>-VAE.

Method	baseline	w/ Hi-CDL	w/ OrthoGate	Ours
PSNR	28.89	29.48	29.32	<b>29.84</b>
SSIM	0.836	0.852	0.853	<b>0.861</b>

mation encoding loss becomes more controllable, allowing degradation-dominated features to be encoded as latent, while background-dominated features are separated during the encoding process. OrthoGate tends to suppress the flow of background-dominated information into deeper encoding layers, while Hi-CDL more precisely captures the degradation patterns. The combined effect of both mechanisms results in the optimal decoupling performance.

## 5.2. Complex Invertible Multiscale Fusion Network

In the ablation study of CIMF-Net, as shown in Tab. 7, we conducted comparisons with the following experimental set-ups: Set1, which is a non-reversible network with a similar number of parameters; Set2, where each scale’s background-dominated features are processed by separate INN networks with no interaction between scales; Set3, which builds on Set2 and introduces cross-attention to enable interaction across scales; and Set4, where the real and imaginary parts of the complex numbers in CIMF-Net are concatenated, fused through convolution, and processed by a real-valued network, with additional INN modules to match CIMF-Net’s parameter count. The results show that CIMF-Net outperforms Set1 in terms of information preservation capability, thanks to its reversibility. Additionally, compared to Set2, Set3, and Set4, CIMF-Net achieves the best performance by leveraging complex-domain operations that facilitate efficient cross-scale interactions.

## 5.3. Latent Restoration Network

We conducted ablation and comparison experiments on LaReNet using three widely used backbones for image restoration: Restormer [37], NAFNet [4], and SFH-

Table 7. Ablation Study of CIMF-Net.

Method	Set1	Set2	Set3	Set4	Ours
PSNR	27.86	29.26	29.52	28.88	<b>29.84</b>
SSIM	0.852	0.857	0.860	0.852	<b>0.861</b>
Params(M)	1.103	2.212	4.289	1.114	<b>1.008</b>

former [11]. The results show that D<sup>2</sup>R-UHDNet achieves excellent performance (PSNR) across all backbones and significantly improves the efficiency (Params, FLOPs, Runtime) and performance of each backbone in UHD restoration tasks. This effectively demonstrates the generalizability of the D<sup>2</sup>R-UHDNet.

## 5.4. Analysis of Information Loss

We visualize the information loss from different downsampling methods as residual maps compared to the GT magnitude spectrum, as shown in Figure 6. It can be observed that traditional information compression methods all face varying degrees of significant information loss. Although DreamUHD alleviates high-frequency information loss through a specialized high-frequency compensation mechanism, the loss of mid-frequency information remains unaddressed. It is evident that, due to the controllability in both the information loss and compensation phases, our method exhibits significantly better information retention compared to other methods. This validates the necessity and effectiveness of the image component decoupling strategy.

Table 8. Ablation Study of LaReNet.

metric	Restormer		NAFNet		SFHformer	
	Base	+D <sup>2</sup> R	Base	+D <sup>2</sup> R	Base	+D <sup>2</sup> R
PSNR (dB)	25.21	29.78/ <b>+4.57</b>	26.06	29.88/ <b>+3.82</b>	25.67	29.84/ <b>+4.17</b>
Param (M)	26.1	3.2/ <b>-87%</b>	29.1	1.6/ <b>-94%</b>	7.6	1.0/ <b>-87%</b>
FLOPS (G)	140.9	6.4/ <b>-95%</b>	16.1	3.9/ <b>-76%</b>	51.0	4.0/ <b>-92%</b>
Runtime (s)	8.8	0.64/ <b>-92%</b>	4.6	0.42/ <b>-92%</b>	5.2	0.44/ <b>-92%</b>
FS	$\times$	✓	$\times$	✓	$\times$	✓

## 6. Conclusion

This paper introduces D<sup>2</sup>R-UHDNet, an efficient and effective framework for UHD image restoration. By decoupling background-dominated and degradation-dominated features and addressing them in a divide-and-conquer manner, the method allows for controllable information loss and targeted information compensation. While maintaining efficiency, it significantly mitigates the information loss typically encountered in traditional UHD restoration methods. The method achieves state-of-the-art results across six experimental settings, including low-light enhancement, dehazing, deblurring, and de-moiréing. The Active Discarding and Targeted Restoration paradigm offers a robust foundation for future advancements in UHD image restoration.

## References

- [1] Gary Becigneul and Octavian-Eugen Ganea. Riemannian adaptive optimization methods. In *International Conference on Learning Representations*. 2, 4
- [2] Jin Cao, Yi Cao, Li Pang, Deyu Meng, and Xiangyong Cao. Hair: Hypernetworks-based all-in-one image restoration, 2024. 8, 2
- [3] Hongming Chen, Xiang Chen, Chen Wu, Zhuoran Zheng, Jinshan Pan, and Xianping Fu. Towards ultra-high-definition image deraining: A benchmark and an efficient method, 2024. 1
- [4] Liangyu Chen, Xiaojie Chu, Xiangyu Zhang, and Jian Sun. Simple baselines for image restoration. In *European conference on computer vision*, pages 17–33. Springer, 2022. 8
- [5] Yuning Cui, Wenqi Ren, Xiaochun Cao, and Alois Knoll. Revitalizing convolutional network for image restoration. *IEEE Transactions on Pattern Analysis and Machine Intelligence*, 2024. 3
- [6] Yuning Cui, Syed Waqas Zamir, Salman Khan, Alois Knoll, Mubarak Shah, and Fahad Shahbaz Khan. Adair: Adaptive all-in-one image restoration via frequency mining and modulation, 2024. 8, 2
- [7] Senyou Deng, Wenqi Ren, Yanyang Yan, Tao Wang, Fenglong Song, and Xiaochun Cao. Multi-scale separable network for ultra-high-definition video deblurring. In *ICCV*, pages 14030–14039, 2021. 6
- [8] Senyou Deng, Wenqi Ren, Yanyang Yan, Tao Wang, Fenglong Song, and Xiaochun Cao. Multi-scale separable network for ultra-high-definition video deblurring. In *the IEEE/CVF International Conference on Computer Vision (ICCV)*, pages 14030–14039, 2021. 1
- [9] Senyou Deng, Wenqi Ren, Yanyang Yan, Tao Wang, Fenglong Song, and Xiaochun Cao. Multi-scale separable network for ultra-high-definition video deblurring. In *ICCV*, pages 14010–14019, 2021. 3
- [10] Hu Gao, Jing Yang, Ning Wang, Jingfan Yang, Ying Zhang, and Depeng Dang. Prompt-based all-in-one image restoration using cnns and transformer. *arXiv preprint arXiv:2309.03063*, 2023. 8, 2
- [11] Xingyu Jiang, Xiuhui Zhang, Ning Gao, and Yue Deng. When fast fourier transform meets transformer for image restoration. In *European Conference on Computer Vision*, pages 381–402. Springer, 2024. 3, 6, 8
- [12] Durk P Kingma and Prafulla Dhariwal. Glow: Generative flow with invertible 1x1 convolutions. *Advances in neural information processing systems*, 31, 2018. 5
- [13] Lingshun Kong, Jiangxin Dong, Jianjun Ge, Mingqiang Li, and Jinshan Pan. Efficient frequency domain-based transformers for high-quality image deblurring. In *2023 IEEE/CVF Conference on Computer Vision and Pattern Recognition (CVPR)*, pages 5886–5895, 2023. 7
- [14] Boyun Li, Xiao Liu, Peng Hu, Zhongqin Wu, Jiancheng Lv, and Xi Peng. All-In-One Image Restoration for Unknown Corruption. In *IEEE Conference on Computer Vision and Pattern Recognition*, New Orleans, LA, 2022. 8, 2
- [15] Chongyi Li, Chun-Le Guo, Man Zhou, Zhixin Liang, Shangchen Zhou, Ruicheng Feng, and Chen Change Loy. Embedding fourier for ultra-high-definition low-light image enhancement. In *ICLR*, 2023. 7, 1
- [16] Chongyi Li, Chun-Le Guo, Man Zhou, Zhixin Liang, Shangchen Zhou, Ruicheng Feng, and Chen Change Loy. Embedding fourier for ultra-high-definition low-light image enhancement. In *ICLR*, 2023. 1, 3, 6
- [17] Yawei Li, Yuchen Fan, Xiaoyu Xiang, Denis Demandolx, Rakesh Ranjan, Radu Timofte, and Luc Van Gool. Efficient and explicit modelling of image hierarchies for image restoration. In *Proceedings of the IEEE/CVF Conference on Computer Vision and Pattern Recognition*, pages 18278–18289, 2023. 3
- [18] Yidi Liu, Dong Li, Jie Xiao, and Xueyang Fu. Dreamuhd: Frequency enhanced variational autoencoder for ultra-high-definition image restoration, 2025. 1, 3, 6, 7, 8, 2
- [19] Vaishnav Potlapalli, Syed Waqas Zamir, Salman Khan, and Fahad Khan. Promptir: Prompting for all-in-one image restoration. In *Thirty-seventh Conference on Neural Information Processing Systems*, 2023. 8, 2
- [20] Yuwei Qiu, Kaihao Zhang, Chenxi Wang, Wenhan Luo, Hongdong Li, and Zhi Jin. Mb-taylorformer: Multi-branch efficient transformer expanded by taylor formula for image dehazing, 2023. 7
- [21] Robin Rombach, Andreas Blattmann, Dominik Lorenz, Patrick Esser, and Björn Ommer. High-resolution image synthesis with latent diffusion models, 2021. 2
- [22] Wenzhe Shi, Jose Caballero, Ferenc Huszár, Johannes Totz, Andrew P Aitken, Rob Bishop, Daniel Rueckert, and Zehan Wang. Real-time single image and video super-resolution using an efficient sub-pixel convolutional neural network. In *Proceedings of the IEEE conference on computer vision and pattern recognition*, pages 1874–1883, 2016. 1
- [23] Yuda Song, Zhuqing He, Hui Qian, and Xin Du. Vision transformers for single image dehazing. *IEEE Transactions on Image Processing*, 32:1927–1941, 2023. 7
- [24] Shangquan Sun, Wenqi Ren, Xinwei Gao, Rui Wang, and Xiaochun Cao. Restoring images in adverse weather conditions via histogram transformer. In *European Conference on Computer Vision*, pages 111–129. Springer, 2025. 8, 2

[25] Fu-Jen Tsai, Yan-Tsung Peng, Yen-Yu Lin, Chung-Chi Tsai, and Chia-Wen Lin. Stripformer: Strip transformer for fast image deblurring. In *European conference on computer vision*, pages 146–162. Springer, 2022. 7

[26] Ziyu Wan, Bo Zhang, Dong Chen, Pan Zhang, Dong Chen, Fang Wen, and Jing Liao. Old photo restoration via deep latent space translation. *IEEE Transactions on Pattern Analysis and Machine Intelligence*, 45(2):2071–2087, 2023. 2

[27] Cong Wang, Jinshan Pan, Wei Wang, Gang Fu, Siyuan Liang, Mengzhu Wang, Xiao-Ming Wu, and Jun Liu. Correlation matching transformation transformers for uhd image restoration. In *Proceedings of the AAAI Conference on Artificial Intelligence*, pages 5336–5344, 2024. 1, 3, 7, 8, 2

[28] Liyan Wang, Cong Wang, Jinshan Pan, Weixiang Zhou, Xiaoran Sun, Wei Wang, and Zhixun Su. Ultra-high-definition restoration: New benchmarks and a dual interaction prior-driven solution, 2024. 7

[29] Liyan Wang, Cong Wang, Jinshan Pan, Weixiang Zhou, Xiaoran Sun, Wei Wang, and Zhixun Su. Ultra-high-definition restoration: New benchmarks and a dual interaction prior-driven solution, 2024. 1, 3, 8, 2

[30] Tao Wang, Kaihao Zhang, Tianrun Shen, Wenhan Luo, Bjorn Stenger, and Tong Lu. Ultra-high-definition low-light image enhancement: A benchmark and transformer-based method. In *Proceedings of the AAAI Conference on Artificial Intelligence*, pages 2654–2662, 2023. 7

[31] Tao Wang, Kaihao Zhang, Ziqian Shao, Wenhan Luo, Bjorn Stenger, Tong Lu, Tae-Kyun Kim, Wei Liu, and Hongdong Li. Gridformer: Residual dense transformer with grid structure for image restoration in adverse weather conditions. *International Journal of Computer Vision*, pages 1–23, 2024. 8, 2

[32] Zhendong Wang, Xiaodong Cun, Jianmin Bao, Wengang Zhou, Jianzhuang Liu, and Houqiang Li. Uformer: A general u-shaped transformer for image restoration. In *Proceedings of the IEEE/CVF Conference on Computer Vision and Pattern Recognition (CVPR)*, pages 17683–17693, 2022. 3, 7

[33] Mingde Yao, Ruikang Xu, Yuanshen Guan, Jie Huang, and Zhiwei Xiong. Neural degradation representation learning for all-in-one image restoration. *IEEE Transactions on Image Processing*, 2024. 8, 2

[34] Ronald Yu. A tutorial on vaes: From bayes’ rule to lossless compression, 2020. 1

[35] Wei Yu, Jie Huang, Bing Li, Kaiwen Zheng, Qi Zhu, Man Zhou, and Feng Zhao. Empowering resampling operation for ultra-high-definition image enhancement with model-aware guidance. In *2024 IEEE/CVF Conference on Computer Vision and Pattern Recognition (CVPR)*, pages 25722–25731, 2024. 1, 7

[36] Xin Yu, Peng Dai, Wenbo Li, Lan Ma, Jiajun Shen, Jia Li, and Xiaojuan Qi. Towards efficient and scale-robust ultra-high-definition image demoiréing. In *European Conference on Computer Vision*, pages 646–662. Springer, 2022. 6, 7

[37] Syed Waqas Zamir, Aditya Arora, Salman Khan, Munawar Hayat, Fahad Shahbaz Khan, and Ming-Hsuan Yang. Restormer: Efficient transformer for high-resolution image restoration. In *CVPR*, 2022. 1, 3, 7, 8

[38] Jinghao Zhang, Jie Huang, Mingde Yao, Zizheng Yang, Hu Yu, Man Zhou, and Feng Zhao. Ingredient-oriented multi-degradation learning for image restoration. In *Proceedings of the IEEE/CVF Conference on Computer Vision and Pattern Recognition*, pages 5825–5835, 2023. 8, 2

[39] Kaihao Zhang, Dongxu Li, Wenhan Luo, Wenqi Ren, Bjorn Stenger, Wei Liu, Hongdong Li, and Yang Ming-Hsuan. Benchmarking ultra-high-definition image super-resolution. In *Proceedings of the IEEE/CVF International Conference on Computer Vision*, 2021. 1

[40] Dian Zheng, Xiao-Ming Wu, Shuzhou Yang, Jian Zhang, Jian-Fang Hu, and Wei-Shi Zheng. Selective hourglass mapping for universal image restoration based on diffusion model. In *Proceedings of the IEEE/CVF Conference on Computer Vision and Pattern Recognition*, pages 25445–25455, 2024. 8, 2

[41] Zhuoran Zheng, Wenqi Ren, Xiaochun Cao, Xiaobin Hu, Tao Wang, Fenglong Song, and Xiuyi Jia. Ultra-high-definition image dehazing via multi-guided bilateral learning. In *CVPR*, pages 16185–16194, 2021. 3, 6

[42] Zhuoran Zheng, Wenqi Ren, Xiaochun Cao, Xiaobin Hu, Tao Wang, Fenglong Song, and Xiuyi Jia. Ultra-high-definition image dehazing via multi-guided bilateral learning. In *2021 IEEE/CVF Conference on Computer Vision and Pattern Recognition (CVPR)*, pages 16180–16189, 2021. 1

[43] Lei Zhou, Chunlei Cai, Yue Gao, Sanbao Su, and Junmin Wu. Variational autoencoder for low bit-rate image compression. In *Proceedings of the IEEE conference on computer vision and pattern recognition workshops*, pages 2617–2620, 2018. 1

[44] Wenbin Zou, Hongxia Gao, Weipeng Yang, and Tongtong Liu. Wave-mamba: Wavelet state space model for ultra-high-definition low-light image enhancement, 2024. 1, 3

# Decouple to Reconstruct: High Quality UHD Restoration via Active Feature Disentanglement and Reversible Fusion

## Supplementary Material

This supplementary document is organized as follows:

Sec. 7 presents additional visual results.

Sec. 8 presents the results under six degradation experimental settings.

Sec. 9 provides the construction of the UHD dataset and details of the experimental setup.

### 7. More visual comparison results.

We present additional visual results for low-light image enhancement, image dehazing, image deblurring, and moiré pattern removal in Figures 7 to 10. As can be observed, our method achieves minimal degradation artifacts while maintaining the consistency of background information in the images.

### 8. The results under six degradation experimental settings

We further design six types of degraded UHD all-in-one experiments, including low-light enhancement, image deblurring, image dehazing, image denoising, image deraining, and image desnowing. The experimental results are shown in Tab. 10. Our method significantly outperforms both traditional all-in-one approaches and UHD restoration methods. By balancing efficiency and performance, we validate the effectiveness of our method.

## 9. Experimental Details

### 9.1. Datasets

The various UHD degradation scenarios in this paper are based on UHD-LL [15], UHD-blur [8], UHD-haze [42], UHD-rain [3], and UHD-snow [29]. For UHD denoising, 4k images from [39] are used as the background. The distributions of the training and testing sets for all datasets are shown in Tab. 9.

### 9.2. Implementation Details

The number of encoder and decoder layers is set to 3, the number of modules in the latent image restoration network is set to 6, and the number of Glow modules in CIMF-Net is set to 3.

For the first stage, we train Clean-VAE on the image reconstruction task. The initial learning rate is set to  $5 \times 10^{-4}$ , gradually reduced to  $1 \times 10^{-7}$  using cosine annealing. The batch size is set to 16, and the images are randomly cropped to  $256 \times 256$ .

In the second stage, we train CD<sup>2</sup>-VAE based on paired degraded-clean image inputs for feature disentanglement training. On one hand, the degraded latent extracted from the input is combined with the clean latent extracted by the Clean-VAE encoder and input into the degraded decoder for the reconstruction of the degraded image. On the other hand, the disentangled background features are input into Clean-VAE’s decoder for the reconstruction of the clean image. The initial learning rate is set to  $5 \times 10^{-4}$ , gradually reduced to  $1 \times 10^{-7}$  using cosine annealing. The batch size is set to 12, and the images are randomly cropped to  $256 \times 256$ .

For the third stage, we train D<sup>2</sup>R-UHDNet on the image restoration task, keeping the parameters of CD<sup>2</sup>-VAE frozen. We fine-tune the parameters of the LaReNet and CIMF-Net. The initial learning rate is set to  $4 \times 10^{-4}$ , gradually reduced to  $1 \times 10^{-7}$  using cosine annealing. The batch size is set to 6, and the images are randomly cropped to  $512 \times 512$ .

### 9.3. Training procedure

In the first phase, Clean-VAE is trained for the image reconstruction task using clean images. The clean input image is denoted as  $I_h$ , and the corresponding reconstructed image is represented as  $I_{r1}$ .

The loss function for a standard Variational Autoencoder (VAE) comprises two key terms: the reconstruction loss and the KL divergence loss. The reconstruction loss quantifies the difference between the decoder’s output and the original input, ensuring the output remains consistent with the input image [34]. The KL divergence loss regularizes the latent space by encouraging the posterior distribution to align with the prior distribution. This regularization improves the model’s ability to generate consistent and continuous reconstructions from similar inputs [43].

We adopt this approach, where the reconstruction loss and KL divergence loss are defined as follows:

$$\begin{aligned} \mathcal{L}_{\text{rec}_1} &= \frac{1}{N} \sum_{i=1}^N \|I_{\text{rl}}^{(i)} - I_{\text{h}}^{(i)}\|_1, \\ \mathcal{L}_{\text{KL}} &= D_{\text{KL}}(q(z|I) \| p(z)), \end{aligned} \quad (11)$$

where  $q(z|I_h)$  represents the approximate posterior distribution of the latent variable  $z$  given the input image  $I_h$ , and  $p(z)$  is the prior distribution, usually chosen as a standard Gaussian distribution  $\mathcal{N}(0, I)$ . The KL divergence  $D_{\text{KL}}$  measures the discrepancy between the posterior distribution  $q(z|I_h)$  and the prior distribution  $p(z)$ .

Additionally, we enforce frequency domain consistency in the reconstruction results using the FFT loss, which is

Table 9. Dataset details and corresponding tasks.

Dataset	Training samples	Testing samples	Task
UHD-Snow	2,000	200	Desnowing
UHD-Blur	1,964	300	Deblurring
UHD-Rain	2,000	500	Deraining
UHD-LL	2,000	115	LLIE
UHD-Haze	2,290	231	Dehazing
UHD-Noise	2,000	500	Denoising

Table 10. Comparison to state-of-the-art on three degradations. PSNR (dB,  $\uparrow$ ), SSIM ( $\uparrow$ ), LPIPS ( $\downarrow$ ) and FS represents full-size 4K image inference. FLOPs are computed for an input size of  $256 \times 256$ . **Best** and **second best** performances are highlighted.

Method	FS	FLOPs	Params.	Low Light		Deblurring		Dehazing		Denoising		Deraining		Desnowing		Average		
				UHD-LL	UHD-blur	UHD-haze	UHDN $_{\sigma=50}$	UHD-rain	UHD-snow									
AIRNet [14]	$\times$	301G	9M	22.68	.887	23.52	.876	18.24	.846	22.38	.876	26.35	.876	27.38	.924	23.43	.874	.1861
IDR [38]	$\times$	88G	15.3M	24.33	.915	25.64	.788	18.68	.879	29.64	.906	28.82	.906	30.48	.945	26.27	.890	.1912
PromptIR [19]	$\times$	158G	33M	23.3	.911	26.48	<b>.805</b>	20.14	.901	24.88	.835	28.89	.897	30.78	.966	25.74	.886	.2155
CAPTNet [10]	$\times$	25G	24.3M	24.97	<b>.921</b>	<b>26.32</b>	.796	<b>20.32</b>	.903	21.64	.569	<b>29.34</b>	<b>.908</b>	<b>32.21</b>	<b>.974</b>	25.80	.845	.2861
NDR-Restore [33]	$\times$	196G	36.9M	25.12	.885	25.64	.791	19.21	.896	31.44	.915	29.24	.897	28.41	.948	26.51	.889	.3108
Gridformer [31]	$\times$	367G	34M	23.92	.898	25.68	.782	18.87	.889	32.86	.915	29.37	.904	28.24	.942	26.49	.895	.2321
DiffUIR-L [40]	$\times$	10G	36.2M	22.64	.902	25.08	.785	18.62	.889	<b>33.25</b>	<b>.928</b>	27.89	.886	27.36	.945	25.81	.889	<b>.1844</b>
Histoformer [24]	$\times$	91G	16.6M	25.73	.915	26.55	.796	18.73	.897	33.05	.924	27.96	.884	27.56	.971	26.59	.898	.1855
adaIR [6]	$\times$	147G	28.7M	23.84	.918	26.86	.803	19.34	<b>.910</b>	32.46	.923	28.18	.901	27.72	.953	26.40	<b>.901</b>	.2492
HAIR [2]	$\times$	41G	29M	<b>25.22</b>	.897	24.77	.799	18.75	.883	32.50	.915	28.76	.893	27.89	.968	26.31	.892	.2607
UHDformer [27]	$\checkmark$	3.0G	0.33M	22.87	.891	24.68	.792	20.02	.888	27.23	.892	28.32	.953	28.24	.882	25.23	.883	.2012
UHDDIP [29]	$\checkmark$	2.2G	0.81M	24.56	.887	24.26	.794	19.68	.872	28.12	.889	28.78	.942	28.07	.893	25.58	.880	.2278
DreamUHD [18]	$\checkmark$	4.1G	1.46M	25.12	.901	25.82	.796	20.21	.908	29.08	.901	30.42	.950	32.12	.914	<b>27.13</b>	.895	.1998
Ours	$\checkmark$	4G	1.0M	<b>26.14</b>	<b>.916</b>	<b>26.87</b>	<b>.799</b>	<b>20.38</b>	<b>.911</b>	<b>29.64</b>	<b>.912</b>	<b>32.28</b>	<b>.968</b>	<b>33.32</b>	<b>.929</b>	<b>28.11</b>	<b>.906</b>	<b>.1842</b>

defined as:

$$\mathcal{L}_{\text{FFT}_1} = \frac{1}{N} \sum_{i=1}^N \|\text{FFT}(I_{\text{rec}}^{(i)}) - \text{FFT}(I_{\text{h}}^{(i)})\|_1. \quad (12)$$

In the second phase, the input degraded image is denoted as  $I_d$ , which corresponds to the clean image  $I_{gt}$ . After feature disentanglement learning with CD<sup>2</sup>-VAE, the degraded image  $I_{d_{\text{rec}}}$  and the clean image  $I_{gt_{\text{rec}}}$  are reconstructed. The same reconstruction loss and frequency loss from the first phase are applied, and they are expressed as follows:

$$\begin{aligned} \mathcal{L}_{\text{rec}_2} &= \frac{1}{N} \sum_{i=1}^N \|I_{d_{\text{rec}}}^{(i)} - I_d^{(i)}\|_1 + \|I_{gt_{\text{rec}}}^{(i)} - I_{gt}^{(i)}\|_1 \\ \mathcal{L}_{\text{FFT}_2} &= \frac{1}{N} \sum_{i=1}^N \|\text{FFT}(I_{d_{\text{rec}}}^{(i)}) - \text{FFT}(I_d^{(i)})\|_1 \\ &\quad + \|\text{FFT}(I_{gt_{\text{rec}}}^{(i)}) - \text{FFT}(I_{gt}^{(i)})\|_1 \end{aligned} \quad (13)$$

In the third phase, the parameters of CD<sup>2</sup>-VAE are frozen, and D<sup>2</sup>R-UHDNet takes over the image restoration task. The input consists only of the degraded image  $I_d$ , and the output of this restoration process is the restored image, denoted as  $I_r$ . The loss function is constructed by comparing the restored image  $I_r$  with the clean ground truth image  $I_{gt}$ , as follows:

$$\begin{aligned} \mathcal{L}_{\text{rec}} &= \frac{1}{N} \sum_{i=1}^N \|I_r^{(i)} - I_{gt}^{(i)}\|_1, \\ \mathcal{L}_{\text{FFT}} &= \frac{1}{N} \sum_{i=1}^N \|\text{FFT}(I_r^{(i)}) - \text{FFT}(I_{gt}^{(i)})\|_1. \end{aligned} \quad (14)$$





Figure 9. Additional visual results for image deblurring.

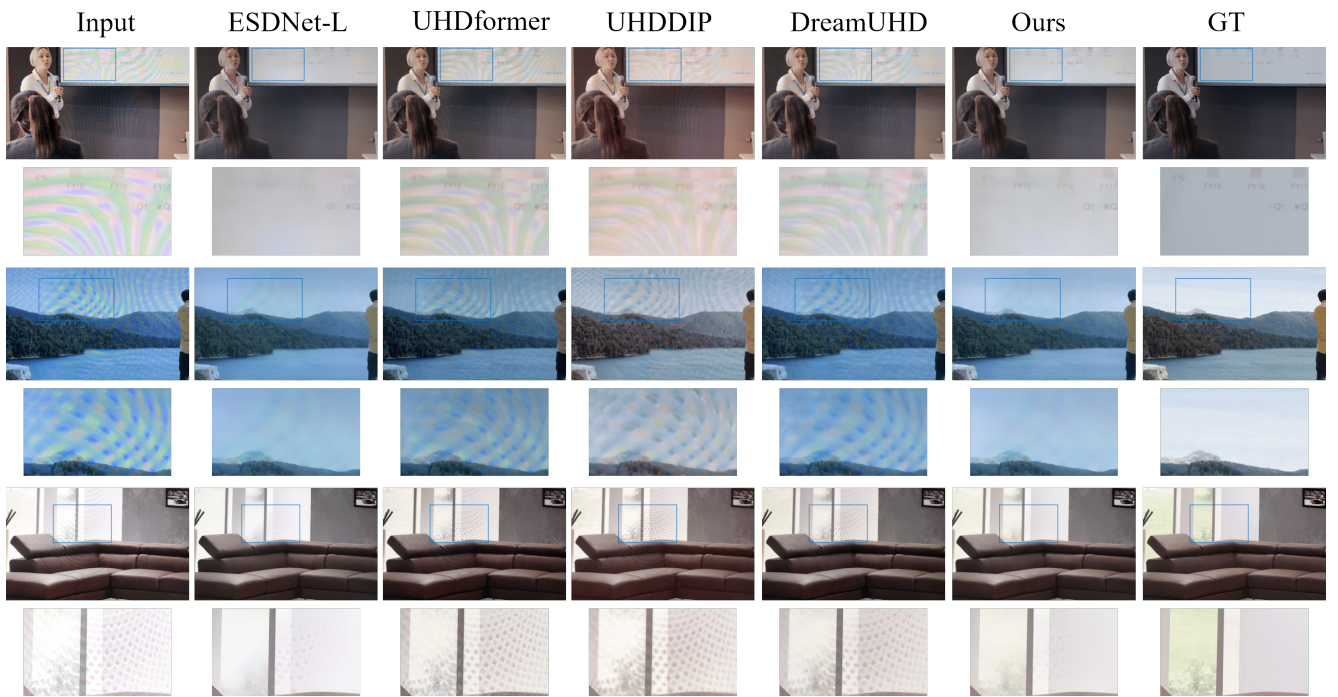


Figure 10. Additional visual results for image demoiring.